

Structure evolution and mechanical properties of hard tantalum diboride films

Cite as: J. Vac. Sci. Technol. A **38**, 033408 (2020); <https://doi.org/10.1116/6.0000155>

Submitted: 26 February 2020 . Accepted: 01 April 2020 . Published Online: 14 April 2020

Viktor Šroba, Tomáš Fiantok, Martin Truchlý, Tomáš Roch, Miroslav Zahoran, Branislav Grančič, Peter Švec, Štefan Nagy, Vitalii Izai, Peter Kúš, and Marián Mikula 



View Online



Export Citation



CrossMark

ARTICLES YOU MAY BE INTERESTED IN

Paradigm shift in thin-film growth by magnetron sputtering: From gas-ion to metal-ion irradiation of the growing film

Journal of Vacuum Science & Technology A **37**, 060801 (2019); <https://doi.org/10.1116/1.5121226>

Strategy for simultaneously increasing both hardness and toughness in ZrB₂-rich Zr_{1-x}Ta_xBy thin films

Journal of Vacuum Science & Technology A **37**, 031506 (2019); <https://doi.org/10.1116/1.5093170>

Review Article: Tracing the recorded history of thin-film sputter deposition: From the 1800s to 2017

Journal of Vacuum Science & Technology A **35**, 05C204 (2017); <https://doi.org/10.1116/1.4998940>



Contact Hiden Analytical for further details:
www.HidenAnalytical.com
info@hiden.co.uk

[CLICK TO VIEW](#) our product catalogue

Instruments for Advanced Science

Gas Analysis



- dynamic measurement of reaction gas streams
- catalytic and thermal analysis
- molecular beam studies
- dissolved species probes
- fermentation, environmental and ecological studies

Surface Science



- UHV TPD
- SIMS
- end point detection in ion beam etch
- elemental imaging - surface mapping

Plasma Diagnostics



- plasma source characterization
- etch and deposition process reaction kinetic studies
- analysis of neutral and radical species

Vacuum Analysis



- partial pressure measurement and control of process gases
- reactive sputter process control
- vacuum diagnostics
- vacuum coating process monitoring


Structure evolution and mechanical properties of hard tantalum diboride films

Cite as: J. Vac. Sci. Technol. A 38, 033408 (2020); doi: 10.1116/6.0000155

Submitted: 26 February 2020 · Accepted: 1 April 2020 ·

Published Online: 14 April 2020



Viktor Šroba,¹ Tomáš Fiantok,² Martin Truchlý,² Tomáš Roch,¹ Miroslav Zahoran,¹ Branislav Grančič,¹ Peter Švec, Jr.,³ Štefan Nagy,⁴ Vitalii Izai,² Peter Kúš,¹ and Marián Mikula^{1,4,a)} 

AFFILIATIONS

¹Department of Experimental Physics, Faculty of Mathematics, Physics and Informatics, Comenius University in Bratislava, Mlynská Dolina F2, 842 48 Bratislava, Slovakia

²Detached Workplace of Faculty of Mathematics, Physics and Informatics, Comenius University in Bratislava, Sadová, 1148 Turany, Slovakia

³Institute of Physics, Slovak Academy of Sciences, Dúbravská cesta 9, 845 11 Bratislava, Slovakia

⁴Institute of Materials and Machine Mechanics SAS, Dúbravská cesta 9, 845 11 Bratislava, Slovakia

^{a)}Electronic mail: marian.mikula@fmph.uniba.sk

ABSTRACT

Tantalum diboride (TaB_2) belonging to the ultrahigh temperature ceramics family is proving to be a promising material for hard protective films, thanks to its high thermal stability and excellent mechanical properties. However, growth of $\text{TaB}_{2 \pm x}$ films prepared using physical vapor deposition techniques is strongly affected by Ar neutrals reflected from a stoichiometric TaB_2 target due to a significant mass difference of heavy Ta and light B atoms leading to substantial changes in the final chemical composition and structure of films. In this work, $\text{TaB}_{2 \pm x}$ films are experimentally prepared using high target utilization sputtering. Stopping and range of ions in matter simulations are used to investigate the behavior of Ar neutrals during deposition processes. A wide range of analytical methods is used to completely characterize the chemical composition, structure, and mechanical properties of $\text{TaB}_{2 \pm x}$ films, and the explanation of the obtained results is supported by density functional theory calculations. $\text{TaB}_{2 \pm x}$ films grow in a broad compositional range from $\text{TaB}_{1.36}$ to $\text{TaB}_{3.84}$ depending on the kinetic energy of Ar neutrals. The structure of overstoichiometric TaB_{2+x} films consists of 0001 preferentially oriented α - TaB_2 nanocolumns surrounded by a boron-tissue phase. In the case of highly understoichiometric TaB_{2-x} films, the boron-tissue phase disappears and the structure consisting of 0001 and 10 $\bar{1}$ 1 oriented α - TaB_2 nanocolumns is formed. All $\text{TaB}_{2 \pm x}$ films exhibit excellent mechanical properties with high hardness, ranging from 27 to 43 GPa and relatively low values of Young's modulus in the range of 304–488 GPa.

Published under license by AVS. <https://doi.org/10.1116/6.0000155>

I. INTRODUCTION

Transition metal diborides (TMB_2) belonging to ultrahigh temperature ceramics are very interesting due to their high temperature chemical stability and excellent mechanical properties. However, the possible high application potential of diboride films is considerably limited in demanding machining processes due to their low oxidation resistance at elevated temperatures and brittle character.^{1–4} In general, TMB_2 crystallize in two different hexagonal structures. Early TMB_2 (e.g., TiB_2 , ZrB_2 , HfB_2 , NbB_2) prefers the so-called α - AlB_2 structure type (space group 191— $P6_3/\text{mmm}$) where α -structure consists of a hexagonal shaped unit cell with an alternating stacking of covalently bonded boron hexagons and metal layers. Late TMB_2

(e.g., MoB_2 , WB_2) form ω - W_2B_5 -x (space group 194— $P6_3/\text{mmc}$) consisting of hexagonal shaped unit cells with alternating flat and puckered boron hexagons between the metal layers.

The preparation of diboride films by physical vapor deposition (PVD) methods such as magnetron sputtering from stoichiometric compounds is accompanied by several interesting aspects. Different angular distributions of sputtered elements play an important role in the formation of under/overstoichiometric nanocomposite films.^{5–8} The well-known overstoichiometric TiB_{2+x} film consists of highly 0001 textured α - TiB_2 nanocolumns surrounded by the B-tissue phase.⁹ In this case, extremely high hardness ($H \sim 50$ GPa) results from the combination of an intrinsically hard TiB_2 phase and cohesive strength between the TiB_2 nanocolumns and the

tissue phase. Similar results were also observed on ZrB_2 films.^{10–12} In addition, thermodynamically nonequilibrium PVD processes led to the synthesis of metastable structures by incorporating point defects such as vacancies, especially in late TM diborides.^{13,14} This effect has been described in several works^{2,10,15–17} as a result of preferential resputtering of boron from the growing films by argon particles. As a result, it is possible to stabilize the α -structure with better mechanical properties in the diborides with the preferred ω -structure.¹³ Moraes *et al.*¹⁴ sputtered slightly understoichiometric α - WB_{2-x} films containing boron vacancies exhibiting a more ductile behavior in comparison with the brittle character of ω - WB_2 . Other authors have presented understoichiometric $\text{MoB}_{1.6}$ (Ref. 18) and $\text{NbB}_{1.7}$ (Ref. 19) films, which, despite boron deficiency, formed vacancy-containing α -nanocolumns surrounded by the B-tissue phase similar to TiB_{2+x} .

Tantalum belongs to very interesting metals from the above-mentioned transition metals of VB and VIB groups due to its high melting temperature, oxidation resistance, and mechanical properties. Tantalum alloying of known nitride films resulted in a significant increase in their thermal stability, enhanced toughness, and improved oxidation resistance by forming a protective Ta_2O_5 film.^{20–24} However, tantalum diboride films represent a lesser-known system. The works by Goncharov *et al.*^{25,26} describe TaB_2 films prepared by RF sputtering without a deeper insight into structure and mechanical properties. Grančič *et al.*⁴ prepared TaB_{2-x} films with direct-current magnetron sputtering from a stoichiometric TaB_2 compound. They drew attention to the significant impact of reflected Ar neutrals (neutralized Ar^+ ions due to secondary electron emission) from heavy Ta atoms in the target toward the growing film. This led to a large resputtering of boron and the formation of a significantly understoichiometric amorphous $\text{TaB}_{1.2}$ film. Only the maximum decrease in acceleration voltage reduced the energy of Ar^+ ions (neutrals) resulting in the nanocrystalline $\text{TaB}_{1.7}$ film but without the typical nanocolumnar character as in other diboride films.

Here, we used stopping and range of ions in matter (SRIM) simulation of sputtering processes and experiments supported by density functional theory (DFT) calculations to investigate the effect of reflected Ar neutrals on the chemical composition, structure, and mechanical properties of tantalum diboride films. $\text{TaB}_{2\pm x}$ films were deposited by high target utilization sputtering (HiTUS) technology where it is possible to independently change the kinetic energy of the argon ions accelerated toward the target (steering of target voltage) while maintaining the same amount (constant target current). The films have grown in a wide compositional range from highly overstoichiometric $\text{TaB}_{3.84}$ to highly understoichiometric $\text{TaB}_{1.36}$, and their structure consists of α - TaB_2 nanocolumnar grains and/or without an amorphous boron-tissue phase. All films exhibited a hardness of >27 GPa, but depending on the stoichiometry, excellent mechanical properties were obtained either by the nanocomposite character of the films or by the boron vacancies-induced hardening.

II. METHODS

A. Experimental details

Experimentally, $\text{TaB}_{2\pm x}$ films $\sim 1\mu\text{m}$ thick were deposited on polished Si (001) and Al_2O_3 (0001) substrates in sputtering

equipment HiTUS (PQL HiTUS Sputter Coating System Model S500, UK) from a sintered stoichiometric TaB_2 target (99.5% purity, 100 mm in diameter, RHP Technology, Austria). Prior to depositions, the substrates were ultrasonically cleaned in acetone, isopropyl alcohol, and rinsed with distilled water. Subsequently, the deposition chamber was pumped on a base pressure of $<3 \times 10^{-3}$ Pa, and Ar^+ cleaning of RF biased substrates (100 W) for 6 min was performed. During the depositions, the gas flow of Ar was kept constant at 100 SCCM leading to a total pressure of 0.66 Pa. High density plasma (10^{12}cm^{-3}) was generated using a remote plasma source with a constant value of RF power at 1500 W. Ar^+ ions were focused on the target using two electromagnetic coils and attracted to the target via pulsed DC power. The values for pulsed DC power on the target were in the range of 200–1000 W (corresponding to a target voltage in the range of 157–840 V and a constant target current of ~ 1.3 A). All depositions were carried out at a floating potential on the substrates heated to a temperature of 400 °C.

Chemical composition of $\text{TaB}_{2\pm x}$ films was determined via scanning electron microscopy using wave dispersive x-ray spectroscopy (WDS, INCA Oxford Instruments) calibrated with a mirror polished sintered TaB_2 standard. In our experience, it is important to note that during WDS analysis impurities on the surface of the films, especially carbon, can significantly distort the measured amount of boron and affect the B/Ta ratio. Therefore, the surface of the samples was treated with an Evactron® XEI Scientific Plasma Decontaminator, and carbon and organic compounds were reduced to a negligible amount. Structure of the films was analyzed by Bragg–Brentano x-ray diffraction (XRD) measurements using a PANalytical X'Pert diffractometer with CuK_α . Detailed studies of the nanostructure of the selected samples were conducted by analytical scanning transmission electron microscopy (STEM) and fast Fourier transformation (FFT) using an FEI Titan operated at 200 kV in high-angle annular dark field (HAADF) and dark field (DF) modes. Specimen preparation was performed in two ways: using a focused ion beam (Tescan Lyra) workstation and by mechanical polishing, dimpling, and Ar^+ -beam polishing using a precision ion polishing system (Gatan). Hardness H and Young's modulus E were measured using a nanoindenter (Anton Paar NHT²) and determined via the Oliver and Pharr method.²⁷

B. Calculation details

DFT calculations performed to support the experimental data were carried out using QUANTUM ESPRESSO v. 6.4.1. employing projector-augmented wave²⁸ pseudopotentials and the Perdew–Burke–Ernzerhof parameterization of the electronic exchange-correlation functionals.^{29,30} Hexagonal α - TaB_{2-x} , $x \in (0, 0.125, 0.25, 0.375, 0.5)$, space group 191 P6/mmm was modeled using supercells constructed as $2 \times 2 \times 2$ α - AlB_2 structure unit (24 atoms) with boron atoms randomly excluded from α - TaB_2 to obtain information about the effect of boron vacancies on the stability of the system. The total energy and structural parameters of five supercell structures with compositions approximately corresponding to five different experimental samples were determined by relaxing cell shapes, volumes, and atomic coordinates using $5 \times 5 \times 5$ k-point grids for Brillouin-zone sampling and a plane wave energy cutoff of

80 eV, while imposing convergence criteria of 10^{-7} eV/atom for forces and 10^{-5} eV/atom for energies. All plane wave energy cutoffs and numbers of k-points were carefully chosen to ensure energy convergence within a few meV/atom. Energies of formation E_f of α -TaB_{2-x} were calculated with respect to mixing cubic (bcc) tantalum, space group 202 F m-3m, and trigonal boron, space group 166, R -3m:H. Charge densities and density of states (DOS) were integrated on $5 \times 5 \times 5$ k-point meshes. Charge densities resolved within energy intervals allowed to identify specific chemical bonds.

III. RESULTS AND DISCUSSION

The involvement of energetic reflected Ar neutrals in sputtering from TaB₂ target using incident Ar⁺ ions was analyzed by simulation software SRIM.³¹ Target used in simulations consisted of Ta and B atoms in a stoichiometric ratio of 1:2 and at a density of 12.51 g cm⁻³. The simulations assume that the energy of incident Ar⁺ ions on target (in electron volts) is equal to the target potential (in volts), and plasma potential, typically a few volts, is neglected. Output of this simulation is energy distribution of reflected Ar neutrals for selected incident ions energies above the target. The calculated output energy distribution described above was subsequently used as an input to SRIM simulation carried out to simulate the transport of reflected Ar neutrals through 20 cm (target-substrate distance in our experiments) in Ar gas with total pressure of 0.66 Pa and background gas temperature of 200 °C, to obtain the energy distribution of reflected Ar neutrals at the substrate position [Fig. 1(a)]. The percentage of reflected Ar neutrals above the target is approximately 14% with respect to the number of impinging Ar⁺ ions. It can be clearly seen that number of reflected Ar neutrals at the substrate position is reduced compared to the target position (8%, 6%, and 4% for 200, 500, and 800 V, respectively); however, the shapes of energy distributions remain constant, and maximum values of energies are only slightly reduced, meaning that a significant number of energetic reflected Ar neutrals at substrate position can strongly affect the chemical composition of growing TaB_{2+x}

films. This effect was observed on magnetron sputtered TaB_{2-x} films where boron resputtering led to the growth of understoichiometric TaB_{1.2} and TaB_{1.7} films.⁴ In comparison, the substantially smaller numbers and values of energies of reflected neutrals were calculated for the well-known TiB₂ target [Fig. 1(b)]. Here, the resputtering of boron is negligible typically leading to the formation of overstoichiometric TiB_{2+x} films.²

WDS analysis of the elemental composition of sputtered TaB_{2+x} films revealed a strong influence of the energy of reflected Ar neutrals on the chemical composition of the growing films in good agreement with SRIM calculations. In Fig. 2, we may observe a significantly overstoichiometric ratio of B/Ta = 3.84 resulting in the composition of TaB_{3.84} that was obtained at the lowest acceleration voltage of 157 V. The effect of boron resputtering is more pronounced with an increase in the energy of accelerated Ar neutrals, when approximately stoichiometric TaB_{2.06} film grows at a voltage of 430 V. A further increase in voltage leads to a monotonic decrease in the B/Ta ratio toward the highly understoichiometric TaB_{1.36} composition at the highest voltages. We also record film contaminations caused by carbon and oxygen impurities not exceeding a total of 5 at. %.

Figure 3 shows a series of XRD 2 θ patterns of deposited TaB_{2+x} films in range between 25° and 60° for 2 θ . As can be seen, the wide range of stoichiometry is also reflected in the phase composition. XRD patterns show relatively broad peaks identified as a crystalline hexagonal α -TaB₂ (space group 191 P6/mmm) phase. Overstoichiometric TaB_{2+x} films exhibit a strong preferred orientation of the α -TaB₂ phase in the 0001 direction which is typical also for other diboride films.^{3,9,12} When the boron content of the films decreases below the B/Ta ratio of <1.7, the strong 0001 preferred orientation disappears and a crystallographically different structure begins to form where, in addition to 0001 highly oriented nanocolumns, some of the nanocolumnar grains grow in the direction 10 $\bar{1}$ 1. This trend is in good agreement with the results for highly understoichiometric magnetron sputtered TaB_{2-x} films.⁴ According to Grančič *et al.*,⁴ a further decrease in the amount of

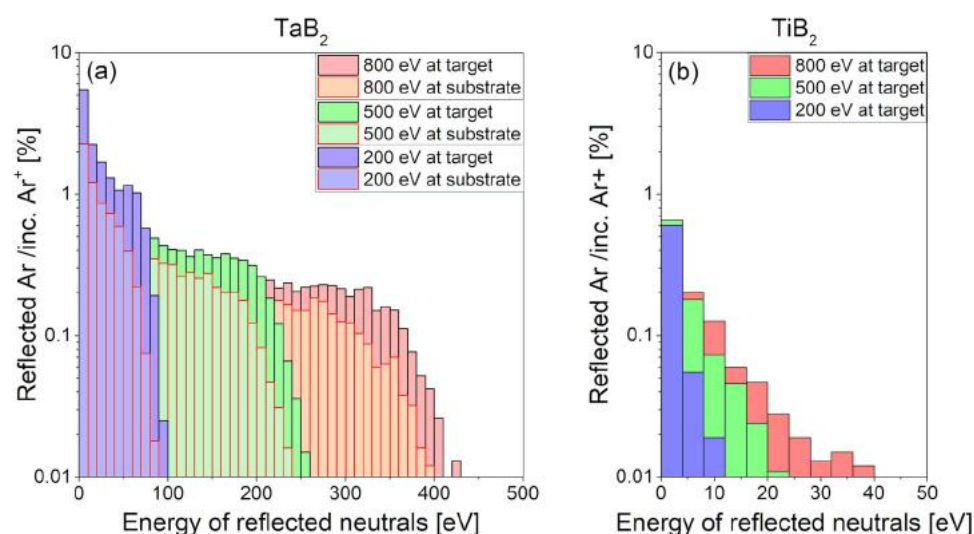


FIG. 1. Energy distribution of reflected Ar neutrals above TaB₂ target position and at the substrate position (lighter color bars) for different energies of incident Ar⁺. (b) Energy distribution of reflected Ar neutrals above the TiB₂ target.

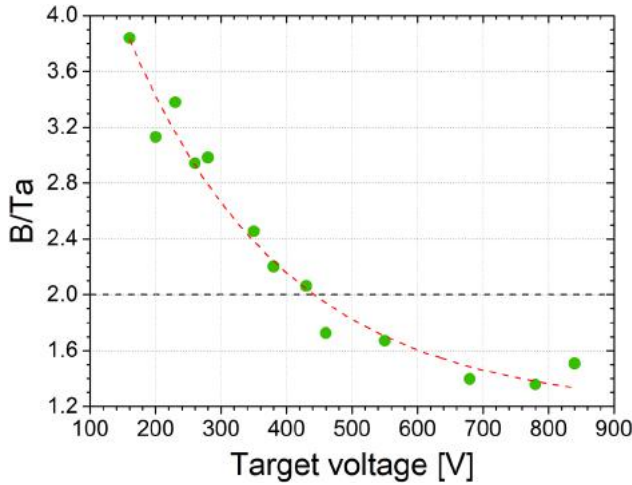


FIG. 2. Boron-to-tantalum (B/Ta) ratio of films plotted as a function of target voltage.

boron in the films leads from the dual structure to the formation of an x-ray amorphous one. We also assume the formation of an x-ray amorphous structure in our TaB_{2-x} films; however, to further reduce the boron content of the films, a higher target voltage than the highest used 840 V would be needed, which unfortunately represents a limit value in our experimental device.

XRD analysis showed that despite the boron deficiency, a hexagonal $\alpha\text{-AlB}_2$ structure type can be formed in understoichiometric TaB_{2-x} films, similar to other TM diborides (TM from the VB and VIB groups). This fact is explained by theoretical approaches where DFT calculations were used to determine the effect of boron vacancies on the energy of formation E_f that directly relates to the stability of the hexagonal $\alpha\text{-TaB}_2$ phase. Here, E_f was calculated by

$$E_f = \frac{1}{\sum_i n_i} \left(E_{\text{tot}} - \sum_i n_i E_i \right), \quad (1)$$

where E_{tot} is total energy of $\alpha\text{-TaB}_2$ and E_i is energy of stable crystalline configuration of n_i atoms for element i . Figure 4(a) shows that increasing the amount of boron vacancies x in the $\alpha\text{-TaB}_{2-x}$ structure results in a decrease of the E_f indicating stabilization of the $\alpha\text{-TaB}_{2-x}$ structure in an understoichiometric state with the most stable composition being approximately $\text{B/Ta} = 1.75$.

To better understand this trend, the electronic structure and chemical bonding analysis were evaluated for TaB_{2-x} . The charge density difference maps illustrating the chemical bonding nature in TaB_2 is depicted in Fig. 5. In Fig. 5(a) across the (0001) plane, there are no localized electrons between neighboring Ta atoms and that bonding in the Ta plane is mainly metallic. In contrast, strong electron localization is evident between neighboring boron atoms on the (0002) plane shown in Fig. 5(b). The B atoms form a graphitelike plane, indicating the covalent nature of the B–B bonds. The Ta–B bonds, shown on (1120) plane, are ionic-covalent [Fig. 5(c)].

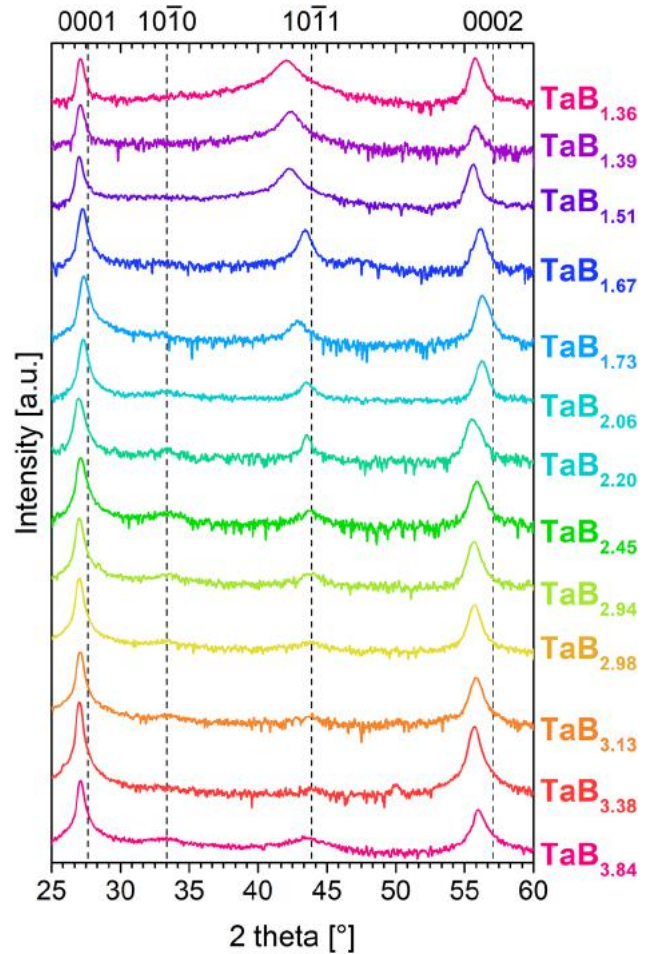


FIG. 3. XRD patterns of as-deposited $\text{TaB}_{2\pm x}$ films as a function of stoichiometry with vertical dashed lines indicating reflections positions for hexagonal $\alpha\text{-TaB}_2$ phase.

As can be seen, the ionic character is shown by the transfer of charge from the Ta to the B atoms. However, a weak interaction is also recognizable between the Ta and B orbital, which also indicates a covalent bond of Ta–B.

Details of bonding characteristics of TaB_{2-x} can be seen from the total DOS shown in Fig. 4(b), where the vertical line indicates the Fermi level E_F . In general, a typical feature of the total DOS of transition metal diborides is the presence of the so-called pseudogap (a sharp valley around the Fermi level). According to Dahlqvist *et al.*,³² the DOS histogram of TaB_2 consists of three parts: (i) the peak at lower energies (~ -14 to -8 eV) belonging to localized B-2s electrons, (ii) the peak around -5 eV due to the bonding states of Ta-d and B-2p electrons, and (iii) above the pseudogap, there are antibonding states dominated by Ta. In the case of known TiB_2 , the number of valence electrons of titanium is four, the valence states are fully filled, and the Fermi level is lying in the pseudogap

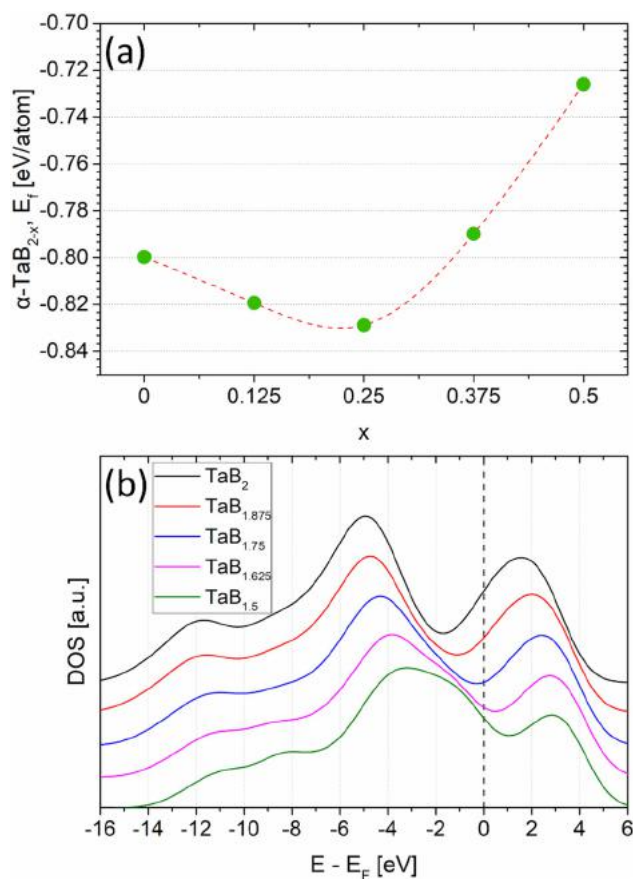


FIG. 4. (a) Energy of formation E_f of α -TaB $_{2-x}$ as a function of boron-vacancy concentration x ; (b) Total DOS of selected boron-vacancy-containing α -TaB $_{2-x}$. The Fermi level is marked by a dotted line at 0 eV.

that confirms high chemical stability of stoichiometric TiB $_2$.³³ In TaB $_2$, the Fermi level is not lying on the pseudogap but above the bottom of antibonding states, indicating that the increased number of valence electrons to five also leads to filling the antibonding states and to a weakening of the chemical stability of TaB $_2$ [black line in Fig. 4(b)]. The introduction of boron vacancies moves E_F toward the minimum of the pseudogap, which is an indication that TaB $_{2-x}$ is stabilized upon the formation of vacancies ($x > 1.625$), which is in a good agreement with the calculated stability in Fig. 4(a). On the other side, the too high number of boron vacancies $x < 1.625$ [the lowest line in Fig. 4(b)] shifts the Fermi level below the top of the bonding states indicating that the valence bands are partially filled and chemical stability of TaB $_2$ is lower.

STEM investigation brings a deeper insight into nanostructure evolution of TaB $_{2 \pm x}$ films (Fig. 6). The STEM-HAADF plane-view image [Fig. 6(a)] of the highly overstoichiometric TaB $_{3.84}$ film reveals a very fine-grained nanostructure consisting of a few nanometer-sized grains. At the same time, the bright and dark areas indicate chemically different regions that are confirmed by

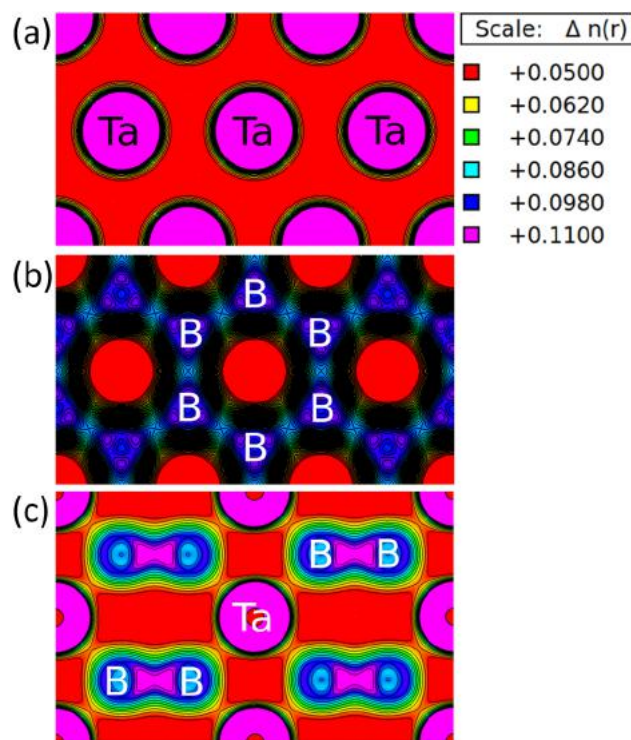


FIG. 5. Charge density maps on (a) (0001) across Ta atoms, (b) (0002) across B atoms, and (c) (1120) across both Ta and B atoms of α -TaB $_2$; a $2 \times 2 \times 2$ supercell was used.

the energy dispersive x-ray spectroscopy (STEM-EDS) analysis. As can be seen in the detail of the nanostructure and elemental maps [inset in Fig. 6(a)], tantalum is found in bright grains, while boron is homogeneously distributed throughout the displayed area. These images confirm the nanocomposite character of the overstoichiometric films formed by TaB $_2$ nanocolumns surrounded by the boron-tissue phase also typical of other TM diborides.^{9,18,19} The circlelike outline of the individual nanocolumns is more pronounced in STEM-HAADF plane-view image of the almost stoichiometric TaB $_{2.06}$ film [Fig. 6(b)]. The diameter of nanocolumns is larger by ~ 5 nm than in the case of overstoichiometric films. The volume fraction of the boron-tissue phase (dark areas) significantly decreases. In STEM-HAADF detail labeled as A [inset in Fig. 6(b)], a well-defined shape of the nanocolumn with recognizable lattice fringes can be seen. The fast Fourier transformation (FFT) pattern obtained from region A shows relatively sharp dots indicating long-range ordering in the selected region. Besides that, the bright dots represent 1010 and $\bar{1}010$ reflections corresponding to the hexagonal α -TaB $_2$ phase.

The nanostructure of understoichiometric TaB $_{2-x}$ films changes significantly with the gradual reduction of boron. The STEM-DF plane-view image of the highly understoichiometric TaB $_{1.39}$ film shows an in-plane increase in the size of nanocolumns. As can be seen, the boron-tissue phase disappears. The interfaces between the nanocolumns are highlighted by a thin dashed line in

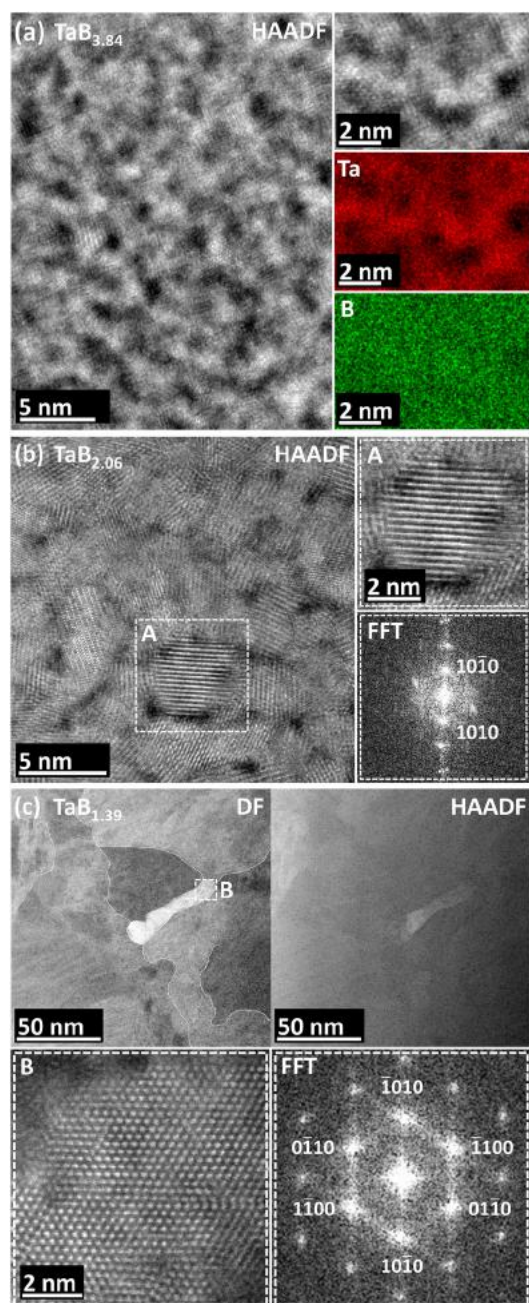


FIG. 6. (a) STEM-HAADF plane-view image of as-deposited highly overstoichiometric $\text{TaB}_{3.84}$ film. The inset in (a) shows STEM-HAADF detail of a very fine-grained nanostructure with corresponding STEM-EDS maps of elemental distributions. (b) STEM-HAADF plane-view image of as-deposited $\text{TaB}_{2.06}$ film showing the circlelike outline of the nanocolumns (in the detail from region A is an individual nanocolumn with the size of a few nanometers) with the corresponding FFT pattern. (c) STEM-DF and STEM-HAADF plane-view images of the as-deposited highly understoichiometric $\text{TaB}_{1.39}$ film showing large nanocolumns formed by the $\alpha\text{-TaB}_2$ phase (FFT pattern obtained from selected region B).

Fig. 6(c). The STEM-HAADF image shows a homogeneous elemental distribution over the entire displayed area. The selected region B plots the presence of the crystalline phase in the nanostructure, and the FFT pattern obtained from region B confirms the presence of the hexagonal $\alpha\text{-TaB}_2$ phase in good agreement with the XRD analysis (Fig. 3). These findings also experimentally confirm the high stability of the hexagonal $\alpha\text{-TaB}_2$ phase containing a large number of boron vacancies in the boron sublattice, as already predicted by DFT calculations [Fig. 4(a)].

The influence of stoichiometry on mechanical properties of $\text{TaB}_{2 \pm x}$ films as a function of target voltage is displayed in Fig. 7(a). As can be seen, the $\text{TaB}_{2 \pm x}$ films are very hard but the way to achieve high hardness values is determined by differences that dominate the structure depending on the chemical composition. A significant increase in hardness was measured in the overstoichiometric films where the lowest hardness of 27.2 ± 1.4 GPa and the highest hardness of 42.4 ± 2.1 GPa exhibited $\text{TaB}_{3.84}$ and $\text{TaB}_{2.98}$, respectively. In addition, a small decrease in hardness to slightly below 40 GPa was observed on the nearly stoichiometric $\text{TaB}_{2.06}$ film. The STEM analysis discussed above revealed the nanocomposite character of these films consisting of oriented nanocolumnar grains and an amorphous B-containing tissue phase, similar to the known TiB_{2+x} .

Also, in our case, the decisive factor determining the hardness is the volume fraction of the amorphous matrix, which the higher the lower the hardness value. Indeed, bonds between atoms from the crystalline and amorphous phases at the interface play an important role in hardening, where the amorphous phase is responsible for the so-called cohesive strength because it acts as a “glue” strongly holding the grains together. Such a system exhibits significant resistance to the penetration of the diamond tip of the indenter and hence high hardness. Mayrhofer *et al.*⁹ reached a hardness of ~ 55 GPa in $\text{TiB}_{2.4}$ films where the thickness of the B-tissue phase surrounding the TiB_2 nanocolumns was only 1–2 monoatomic layers (MLs). Veprek³⁴ reported similar results in a Ti–Si–N nanocomposite system consisting of TiN nanocrystallites with a typical size of 3–4 nm and SiN_x interfacial layer. The thickness of the SiN_x layer determined the hardness values where the highest hardness of about 60 GPa was achieved at a thickness of 1 ML. In this case, very strong shear-resistant bonds are formed at the interface between TiN nanocrystallites and SiN_x . However, with the increasing thickness of the SiN_x layer (2 ML), the cohesive strength decreases significantly resulting in a reduction in hardness.^{34,35} From this point of view, the highest hardness of ~ 42 GPa achieved in $\text{TaB}_{2.98}$ is the result of the optimal thickness of the B-tissue phase where the cohesive strength at the interface between the crystalline and amorphous phases is highest.

Furthermore, in the case of the understoichiometric films, the hardness values are higher than 40 GPa and do not change significantly [Fig. 7(a)]. As explained by the STEM investigation, boron deficiency causes the gradual disappearance of the B-tissue phase [Fig. 6(c)] as well as the formation of boron vacancies in the crystalline $\alpha\text{-TaB}_2$ phase, which, however, stabilize the hexagonal structure at a certain concentration. In Fig. 7(b) showing the charge density difference maps, one can see that the presence of boron vacancy in the sublattice causes the strengthening of ion-covalent

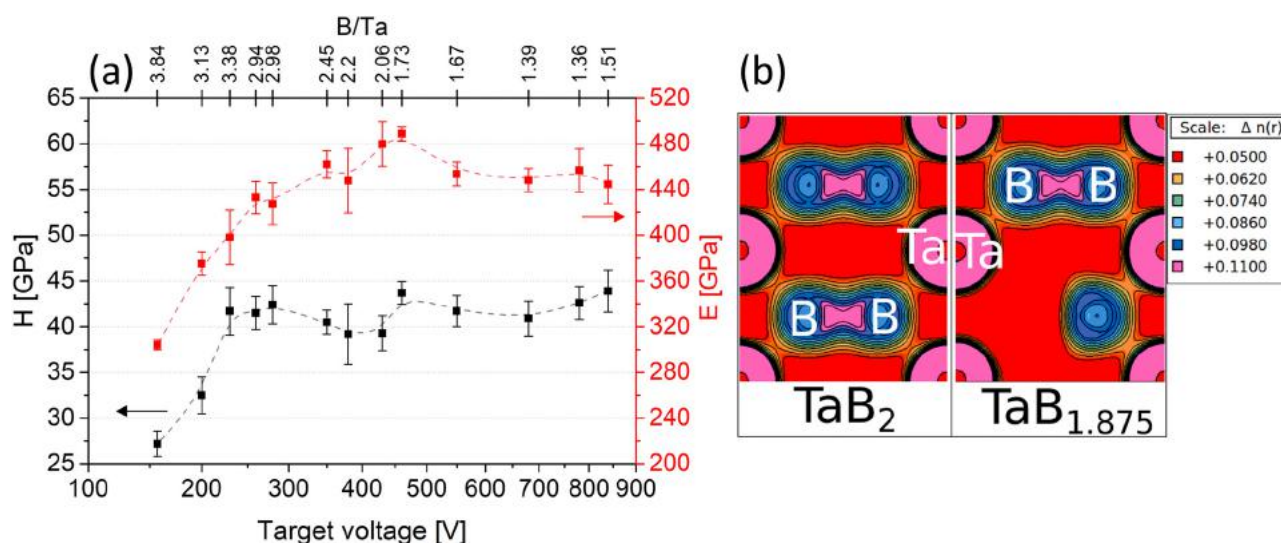


FIG. 7. (a) Hardness and Young's modulus values of TaB_{2+x} films shown as a function of target voltage with top x-axis depicting the B/Ta ratio of the films. (b) Comparison of charge density maps on 1120 planes for TaB_2 (on the left) and $\text{TaB}_{1.875}$ with boron vacancy (on the right).

bonds between the neighboring boron and tantalum atoms, which may have a positive effect on hardness values. The highest hardness value of 43.7 ± 1.9 GPa was measured on $\text{TaB}_{1.73}$, which can be attributed to vacancy-induced hardening. It is important to note that the preferred grain orientation and size, which vary with decreasing boron content, have some effect on hardness in all films. However, their proportion is difficult to distinguish.

The value of Young's modulus E of $\text{TaB}_{3.84}$ with the largest boron content is relatively low, 304 ± 4.3 GPa, and is apparently strongly influenced by the elastic properties of the boron-containing tissue phase [Fig. 7(a)]. The volume reduction of the amorphous matrix and the dominance of the crystalline phase are manifested by a gradual increase in the values of elastic modulus. Young's modulus of 479.9 ± 19.6 GPa of the nearly stoichiometric $\text{TaB}_{2.06}$ film is in good agreement with the theoretical predictions of Zhou *et al.*,³³ who calculated E of 497 GPa for TaB_2 . The elastic behavior of the understoichiometric films is primarily determined by the amount of boron vacancies in the TaB_2 nanocolumns where a large amount of them lead to weakening of the strong Ta–B bonds and Young's modulus decreases ($E = 453.5 \pm 10.4$ GPa for $\text{TaB}_{1.67}$). At the same time, according to XRD analysis (Fig. 3), the preferential orientation of the crystalline phase of the films change from 0001 to 10 $\bar{1}$ 1. According to Xu *et al.*³⁶ and Shein and Ivanovskii,³⁷ diborides for VB group metals show a moderate anisotropy of linear compressibility along the a - and c -axes. Thus, Young's moduli expressing the stiffness in the lattice are different in individual crystallographic directions. This fact could also be attributed to the resulting values of Young's moduli of the highly understoichiometric films. However, a more detailed explanation of the elastic behavior requires a deeper theoretical analysis of electron structures and their effect on the elastic properties of TaB_{2-x} , which is beyond the scope of this work.

IV. CONCLUSIONS

To conclude, we demonstrate the effect of reflected Ar neutrals on the chemical composition, structure, and mechanical properties of TaB_{2+x} films deposited using HiTUS. Influencing kinetic energy of Ar neutrals that cause resputtering of the light boron from the growing films via target voltage leads to the formation of TaB_{2+x} films over a wide concentration range (B/Ta from 3.84 to 1.36). Overstoichiometric TaB_{2+x} films have a nanocomposite structure consisting of 0001 preferentially oriented crystalline α - TaB_2 nanocolumns surrounded by a B-tissue phase. As the boron content gradually decreases, the structure of the films changes, the B-tissue phase disappears, and α - TaB_2 nanocolumns simultaneously grow in 0001 and 10 $\bar{1}$ 1 crystallographic directions. At the same time, it has been shown that the crystalline α - TaB_2 phase is still present in the understoichiometric TaB_{2-x} films, since a certain number of boron vacancies in the boron sublattice promotes its stability. All films exhibit excellent mechanical properties when they reached high hardness values in the range of ~27 to ~43 GPa and Young's modulus ranging from 304 to 488 GPa depending on the stoichiometry. The decisive factor determining the mechanical properties is in the case of overstoichiometric films, their nanocomposite character, the volume fraction of the B-tissue phase, and the cohesion strength between the crystalline nanocolumns and the B-tissue phase. On the other hand, boron vacancies-induced hardening dominates in slightly understoichiometric films, when ion-covalent Ta–B bonds are strengthened, resulting in highest hardness values of >40 GPa.

Our results suggest that using suitable deposition parameters, it is possible to sputter TaB_{2+x} films with defined mechanical properties and tailor them for specific engineering applications.

ACKNOWLEDGMENTS

This work was supported by the Slovak Research and Development Agency (Grant No. APVV-17-0320), Scientific Grant Agency (Grant No. VEGA 1/0381/19), and Operational Program Research and Development (Project No. ITMS 26210120010).

REFERENCES

- ¹P. H. Mayrhofer, C. Mitterer, J. G. Wen, I. Petrov, and J. E. Greene, *J. Appl. Phys.* **100**, 044301 (2006).
- ²M. Mikula *et al.*, *Vacuum* **85**, 866 (2011).
- ³M. Mikula, B. Grančič, V. Buršíková, A. Csuba, M. Držík, Š. Kavecký, A. Plecenik, and P. Kúš, *Vacuum* **82**, 278 (2007).
- ⁴B. Grančič *et al.*, *Surf. Coat. Technol.* **367**, 341 (2019).
- ⁵J. Neidhardt, S. Mráz, J. M. Schneider, E. Strub, W. Bohne, B. Liedke, W. Möller, and C. Mitterer, *J. Appl. Phys.* **104**, 063304 (2008).
- ⁶I. Petrov *et al.*, *J. Vac. Sci. Technol. A* **35**, 050601 (2017).
- ⁷B. Bakhit, I. Petrov, J. E. Greene, L. Hultman, J. Rosén, and G. Greczynski, *J. Vac. Sci. Technol. A* **36**, 030604 (2018).
- ⁸H. Euchner, P. H. Mayrhofer, H. Riedl, F. F. Klimashin, A. Limbeck, P. Polcik, and S. Kolozsvári, *Acta Mater.* **101**, 55 (2015).
- ⁹P. H. Mayrhofer, C. Mitterer, J. G. Wen, J. E. Greene, and I. Petrov, *Appl. Phys. Lett.* **86**, 131909 (2005).
- ¹⁰L. Tengdelius, J. Birch, J. Lu, L. Hultman, U. Forsberg, E. Janzén, and H. Högberg, *Phys. Status Solidi A* **211**, 636 (2014).
- ¹¹L. Tengdelius, G. Greczynski, M. Chubarov, J. Lu, U. Forsberg, L. Hultman, E. Janzén, and H. Högberg, *J. Cryst. Growth* **430**, 55 (2015).
- ¹²L. Tengdelius, E. Broitman, J. Lu, F. Eriksson, J. Birch, T. Nyberg, L. Hultman, and H. Högberg, *Acta Mater.* **111**, 166 (2016).
- ¹³V. Moraes, H. Riedl, C. Fuger, P. Polcik, H. Bolvardi, D. Holec, and P. H. Mayrhofer, *Sci. Rep.* **8**, 9288 (2018).
- ¹⁴V. Moraes, C. Fuger, V. Paneta, D. Primetzhofner, P. Polcik, H. Bolvardi, M. Arndt, H. Riedl, and P. H. Mayrhofer, *Scr. Mater.* **155**, 5 (2018).
- ¹⁵S.-T. Lin and C. Lee, *J. Electrochem. Soc.* **150**, G607 (2003).
- ¹⁶D. B. Bergstrom, F. Tian, I. Petrov, J. Moser, and J. E. Greene, *Appl. Phys. Lett.* **67**, 3102 (1995).
- ¹⁷M. Rudolph, D. Lundin, E. Foy, M. Debonnie, M.-C. Hugon, and T. Minea, *Thin Solid Films* **658**, 46 (2018).
- ¹⁸P. Malinovskis, J. Palisaitis, P. O. Å. Persson, E. Lewin, and U. Jansson, *J. Vac. Sci. Technol. A* **34**, 031511 (2016).
- ¹⁹N. Nedfors, O. Tengstrand, J. Lu, P. Eklund, P. O. Å. Persson, L. Hultman, and U. Jansson, *Surf. Coat. Technol.* **257**, 295 (2014).
- ²⁰M. Mikula, M. Truchlý, D. G. Sangiovanni, D. Plašienka, T. Roch, M. Gregor, P. Ďurina, M. Janík, and P. Kúš, *J. Vac. Sci. Technol. A* **35**, 060602 (2017).
- ²¹M. Mikula *et al.*, *Surf. Coat. Technol.* **288**, 203 (2016).
- ²²R. Hollerweger, H. Riedl, J. Paulitsch, M. Arndt, R. Rachbauer, P. Polcik, S. Primig, and P. H. Mayrhofer, *Surf. Coat. Technol.* **257**, 78 (2014).
- ²³R. Hollerweger *et al.*, *Acta Mater.* **83**, 276 (2015).
- ²⁴J. Musil, J. Vlček, and P. Zeman, *Adv. Appl. Ceram.* **107**, 148 (2008).
- ²⁵A. A. Goncharov, P. I. Ignatenko, V. A. Kononov, V. A. Stupak, G. K. Volkova, V. A. Glazunova, and V. V. Petukhov, *Phys. Metals Metallogr.* **103**, 77 (2007).
- ²⁶A. A. Goncharov, A. V. Zykov, I. V. Shelest, A. N. Yunda, S. D. Yakovin, V. N. Kuznetsov, A. D. Mikhalev, and V. V. Buranich, *2016 International Conference on Nanomaterials: Application & Properties (NAP)*, Lviv, Ukraine, 14–19 September 2016 (IEEE, New York, 2016), pp. 01PCSI08-1–01PCSI08-4.
- ²⁷W. C. Oliver and G. M. Pharr, *J. Mater. Res.* **7**, 1564 (1992).
- ²⁸P. E. Blöchl, *Phys. Rev. B* **50**, 17953 (1994).
- ²⁹P. Giannozzi *et al.*, *J. Phys. Condens. Matter* **21**, 395502 (2009).
- ³⁰P. Giannozzi *et al.*, *J. Phys. Condens. Matter* **29**, 465901 (2017).
- ³¹J. F. Ziegler, M. D. Ziegler, and J. P. Biersack, *Nucl. Instrum. Met. Phys. Res. Sect. B* **268**, 1818 (2010).
- ³²M. Dahlqvist, U. Jansson, and J. Rosen, *J. Phys. Condens. Matter* **27**, 435702 (2015).
- ³³Y. Zhou, H. Xiang, Z. Feng, and Z. Li, *J. Mater. Sci. Technol.* **31**, 285 (2015).
- ³⁴S. Veprek, *J. Vac. Sci. Technol. A* **31**, 050822 (2013).
- ³⁵R. F. Zhang, A. S. Argon, and S. Veprek, *Phys. Rev. B* **79**, 245426 (2009).
- ³⁶X. Xu, K. Fu, M. Yu, Z. Lu, X. Zhang, G. Liu, and C. Tang, *J. Alloys Compd.* **607**, 198 (2014).
- ³⁷I. R. Shein and A. L. Ivanovskii, *J. Phys. Condens. Matter* **20**, 415218 (2008).